NANO EXPRESS   **Open Access**

CrossMark

Self-templated Synthesis of Nickel Silicate Hydroxide/Reduced Graphene Oxide Composite Hollow Microspheres as Highly Stable Supercapacitor Electrode Material

Yanhua Zhang, Wenjie Zhou, Hong Yu, Tong Feng, Yong Pu, Hongdong Liu, Wei Xiao[*] and Liangliang Tian[*]

Abstract

Nickel silicate hydroxide/reduced graphene oxide ($Ni_3Si_2O_5(OH)_4$/RGO) composite hollow microspheres were one-pot hydrothermally synthesized by employing graphene oxide (GO)-wrapped SiO_2 microspheres as the template and silicon source, which were prepared through sonication-assisted interfacial self-assembly of tiny GO sheets on positively charged SiO_2 substrate microspheres. The composition, morphology, structure, and phase of $Ni_3Si_2O_5(OH)_4$/RGO microspheres as well as their electrochemical properties were carefully studied. It was found that $Ni_3Si_2O_5(OH)_4$/RGO microspheres featured distinct hierarchical porous morphology with hollow architecture and a large specific surface area as high as 67.6 m^2 g^{-1}. When utilized as a supercapacitor electrode material, $Ni_3Si_2O_5(OH)_4$/RGO hollow microspheres released a maximum specific capacitance of 178.9 F g^{-1} at the current density of 1 A g^{-1}, which was much higher than that of the contrastive bare $Ni_3Si_2O_5(OH)_4$ hollow microspheres and bare RGO material developed in this work, displaying enhanced supercapacitive behavior. Impressively, the $Ni_3Si_2O_5(OH)_4$/RGO microsphere electrode exhibited outstanding rate capability and long-term cycling stability and durability with 97.6% retention of the initial capacitance after continuous charging/discharging for up to 5000 cycles at the current density of 6 A g^{-1}, which is superior or comparable to that of most of other reported nickel-based electrode materials, hence showing promising application potential in the energy storage area.

Keywords: Nickel silicate hydroxide, Graphene, Hollow structure, Supercapacitor, Self-template, Hydrothermal synthesis

Background

To ease the energy crisis and environmental problems, there is an important and urgent need to develop clean and sustainable power sources as well as advanced energy conversion and storage devices [1]. Supercapacitors, usually known as electrochemical capacitors, have attracted tremendous attention owing to their higher energy density than traditional dielectric capacitors, higher power density than batteries, rapid charge/discharge rate, and quite long cycle life [2]. The exploration of high-performance electrode materials is a crucial challenge for the construction and application of supercapacitors. Up to now, a large number of supercapacitor electrode materials with different components, morphologies, and architecture such as

nanostructured carbonaceous matter (e.g., porous carbon, graphene network, carbon nanotubes), metal sulfides (e.g., MoS_2, Ni_3S_2, WS_2), metal oxides (e.g., MnO_2, RuO_2, CeO_2), metal hydroxides (e.g., $Co(OH)_2$, $Ni(OH)_2$), conducting polymers (e.g., polyaniline, polypyrrole), and their hybrid composites have been well fabricated [2–8]. Unfortunately, most of them suffer from one or more problems like high cost, complicated preparative process, limited specific capacitance, unsatisfactory cycling stability, and low rate capability. Among these disadvantages, the inferior cycling stability is particularly acute, which severely restricts their further practical applications in the supercapacitor field [9]. Consequently, it remains a challenging task to develop highly stable electrode materials with excellent supercapacitive behavior through facile and cost-effective strategies.

As a typical member of metal silicate hydroxides, nickel silicate hydroxide ($Ni_3Si_2O_5(OH)_4$) has a layered structure

* Correspondence: showame@aliyun.com; tianll07@163.com
Research Institute for New Materials Technology, Chongqing University of Arts and Sciences, Yongchuan, Chongqing 402160, China

Zhang *et al. Nanoscale Research Letters* (2017) 12:325

Page 2 of 11

formed by outer octahedral $Ni(II)O_6$ sheets and inner tetrahedral SiO_4 sheets [10]. Thanks to the earth abundance and environmental friendliness, $Ni_3Si_2O_5(OH)_4$ has been widely utilized as adsorbents for heavy metal ions and organic dyes, carriers for drug release, molecular sieves, and catalyst supports [10–14]. However, its application as electroactive materials is quite limited because of its intrinsic poor electronic conductivity [10]. Despite this drawback, the layered structure of $Ni_3Si_2O_5(OH)_4$ still endows it with an appealing feature for electrochemical applications, since such structure could provide numerous well-defined multichannels for fast mass transfer, which is a critical factor during electrochemical reactions [10]. To improve the conductivity of $Ni_3Si_2O_5(OH)_4$-based materials, hybridization of $Ni_3Si_2O_5(OH)_4$ with a conductive matrix including reduced graphene oxide and carbon nanotubes has been recently achieved, and the resulting composites were successfully used in electrocatalytic water oxidation and lithium-ion batteries [10, 15–17]. Nevertheless, the report with respect to the application of $Ni_3Si_2O_5(OH)_4$-based materials in supercapacitor remains rare.

Graphene, a single layer of graphite, has been regarded as one of the most promising materials due to its attractive physicochemical properties and functions like light weight, exceptional electronic conductivity, and splendid chemical stability [17]. Accordingly, integration of graphene or reduced graphene oxide (RGO) with other inorganic species to boost electrochemical behavior has become an effective strategy, and a variety of graphene- or RGO-containing hybrids (e.g., hollow-structured MoS_2/RGO microspheres, RGO-wrapped polyaniline nanowires, nanocubic Co_3O_4/ RGO composites) with reinforced supercapacitive performance have been explored as well [4, 18, 19]. Over the past few years, self-assembly of graphene oxide (GO) sheets on solid substrates via electrostatic interaction has been demonstrated to be a versatile way to prepare GO- and RGO-based composites [20]. By means of this methodology, we have pioneered the fabrication of highly water-dispersible GO-encapsulated SiO_2 microspheres (Fig. 1). The excellent aqueous dispersity of the resultant SiO_2/GO composite microspheres enabled them to be readily modified or treated for further functionalization [4, 21, 22]. Herein, we take advantage of this point and utilize them as the template and silicon source to prepare flower-like nickel silicate hydroxide/reduced graphene oxide ($Ni_3Si_2O_5(OH)_4$/RGO) composite hollow microspheres with a hierarchical porous structure in one pot. As illustrated in Fig. 1, SiO_2/GO microspheres underwent a hydrothermal process in the presence of polyvinylpyrrolidone, nickel nitrate, and urea, during which the SiO_2 inner core reacted with nickel cations to produce $Ni_3Si_2O_5(OH)_4$ in alkaline condition and its deposition, growth, and crystallization on substrate microspheres together with the reduction of GO to RGO were synchronously accomplished, giving rise to the final product of $Ni_3Si_2O_5(OH)_4$/RGO composite hollow microspheres. When employed as a supercapacitor electrode material, the synthesized $Ni_3Si_2O_5(OH)_4$/RGO microspheres released a maximum specific capacitance of 178.9 F g^{-1} at the current density of 1 A g^{-1} in a three-electrode system and maintained 97.6% of the initial capacitance after repetitive charging/discharging at the current of 6 A g^{-1} over 5000 cycles, exhibiting outstanding long-term cycling stability and durability.

Methods
Materials and Reagents
Ammonium hydroxide (25 wt%), tetraethyl orthosilicate, poly(diallyldimethylammonium) chloride (PDDA), nickel nitrate hexahydrate, urea, polyvinylpyrrolidone (PVP) with an average molecular weight of 40,000, acetylene black, *N*-methyl-2-pyrrolidone (NMP), nickel foam, potassium hydroxide, and polyvinylidene fluoride (PVDF) were purchased from J&K Co., Ltd. (Shanghai, China). Commercial tiny GO sheets with the lateral size less than 200 nm were provided by Nanjing JCNANO Technology Co., Ltd. (Nanjing, China). All other chemicals were guaranteed reagents and directly used as received.
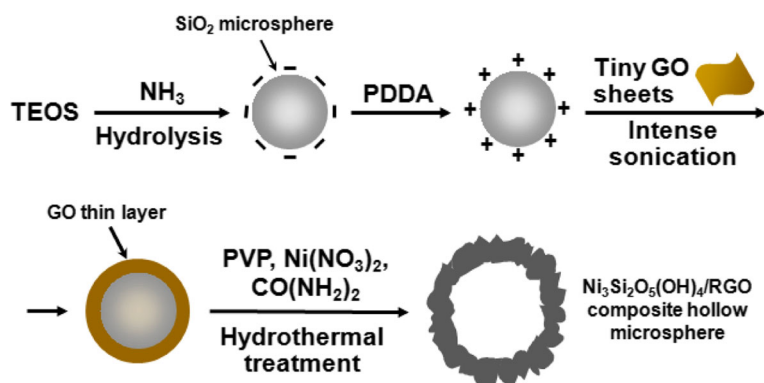
Fig. 1 Schematic representation of the fabrication of hierarchical flower-like $Ni_3Si_2O_5(OH)_4$/RGO composite hollow microspheres

Zhang et al. Nanoscale Research Letters (2017) 12:325

Page 3 of 11

Synthesis of Ni$_3$Si$_2$O$_5$(OH)$_4$/RGO Composite Hollow Microspheres

Monodisperse colloidal SiO$_2$ microspheres with the diameter of ~300 nm were first prepared based on a modified Stöber method (see Additional file 1 for experimental details). Subsequently, GO-encapsulated SiO$_2$ microspheres (i.e., SiO$_2$/GO composite microspheres) were fabricated by sonication-assisted interfacial self-assembly of tiny GO sheets on cationic polyelectrolyte-decorated SiO$_2$ microspheres (i.e., PDDA-modified SiO$_2$ microspheres) through electrostatic interaction (see Additional file 1 for experimental details). Ni$_3$Si$_2$O$_5$(OH)$_4$/RGO hollow microspheres were one-step hydrothermally synthesized through a self-template route. Typically, 20 mg of SiO$_2$/GO microspheres were dispersed in 12 mL of water, followed by introduction of 8 mL of mixed aqueous solution containing 80 mg of nickel nitrate hexahydrate, 0.6 g of PVP, and 1 g of urea under sonication. The resulting reaction mixture was then poured into a stainless autoclave (50 mL of capacity) and sealed, which was subsequently allowed to undergo a hydrothermal reaction at 180 °C for 12 h. During the hydrothermal process, SiO$_2$ reacted with nickel ions and urea to yield Ni$_3$Si$_2$O$_5$(OH)$_4$, which was grown on the substrate microspheres. At the same time, the GO component was hydrothermally reduced to RGO, hence resulting in the generation of flower-like Ni$_3$Si$_2$O$_5$(OH)$_4$/RGO composite hollow microspheres in one pot. After that, the product was separated and washed with abundant water, followed by drying and annealing at 600 °C for 2 h in Ar atmosphere. To demonstrate the role of PVP in the hydrothermal synthetic system, a Ni$_3$Si$_2$O$_5$(OH)$_4$/RGO hybrid material was similarly synthesized according to the above procedure but without the introduction of PVP. As control, contrastive bare Ni$_3$Si$_2$O$_5$(OH)$_4$ hollow microspheres were hydrothermally fabricated by using pure SiO$_2$ microspheres as the template, followed by the same annealing treatment. In addition, bare RGO material was also prepared through hydrothermal reduction of tiny GO sheets at 180 °C for 12 h.

Characterizations

Powder X-ray diffraction (XRD) patterns with the scanning range from 10° to 70° were obtained on a Bruker D8 ADVANCE diffractometer. Field emission scanning electron microscopy (FESEM) inspection was performed on a Hitachi SU8010 microscope working at the acceleration voltage of 3 kV. Transmission electron microscopy (TEM) observation was carried out on a JEOL JEM-2100F microscope operating at the acceleration voltage of 200 kV and equipped with an energy-dispersive spectroscopy (EDS) system. X-ray photoelectron spectra (XPS) were recorded on a VG ESCALAB MARK II instrument. Raman spectra were collected from a HORIBA Scientific Raman spectrometer with the excitation source of 532-nm laser line.

Nitrogen adsorption–desorption isotherms were recorded on a Micromeritics ASAP 2020 apparatus at –196 °C, and the specific surface area of the samples was calculated by the Brunauer–Emmett–Teller (BET) model.

Electrochemical Measurements

All the electrochemical tests were done on a CHI 760E electrochemical workstation (CH Instruments, Inc., Shanghai, China) with a three-electrode system by employing aqueous solution of 2 M KOH as the electrolyte. Hg/HgO electrode, platinum foil, and nickel foam substrate coated with active material were used as the reference electrode, counter electrode, and working electrode, respectively. To fabricate the working electrode, the active material was mixed with acetylene black and PVDF at the weight ratio of 80:10:10. Then, NMP was added into the mixture, followed by gentle grinding to generate a homogeneous slurry. After that, the resulting slurry was pasted onto a nickel foam current collector with the area of 1 cm × 1 cm, followed by drying at 60 °C overnight in a vacuum oven, and the loading amount of active material on the working electrode was ~2.5 mg. Cyclic voltammetry (CV) curves were recorded in the potential window between 0.15 and 0.65 V at various scanning rates. Galvanostatic charge/discharge (GCD) measurements were done in the potential range from 0.2 to 0.6 V at a series of current densities. Electrochemical impedance spectroscopy (EIS) was carried out in the frequency range from 0.01 to 100,000 Hz at open-circuit potential with an ac perturbation of 5 mV.

Results and Discussion
Material Characterizations

Figure 2a and Additional file 1: Figure S1a, b are the FESEM images of pure monodisperse SiO$_2$ microspheres with the diameter of ~300 nm and a perfect smooth surface, displaying white color (inset of Fig. 2a). Figure 2b and Additional file 1: Figure S1c, d present the FESEM images of SiO$_2$/GO microspheres, whose size seems to be unchanged as compared with SiO$_2$ microspheres while whose apparent color becomes yellow brown (inset of Fig. 2b). Also, the outer surface of SiO$_2$/GO microspheres seems to be slightly rougher and some twisted crumples can be identified (Fig 2b and Additional file 1: Figure S1d), which should arise from the encapsulation of tiny GO sheets on substrate microspheres. These results confirm the successful sonication-assisted interfacial self-assembly of tiny GO sheets on the positively charged SiO$_2$ microspheres by virtue of electrostatic interaction. Ni$_3$Si$_2$O$_5$(OH)$_4$/RGO composite hollow microspheres were one-pot prepared by hydrothermal treatment of the SiO$_2$/GO microsphere template in the presence of nickel nitrate, urea, and PVP, and their morphology was carefully inspected. Compared with
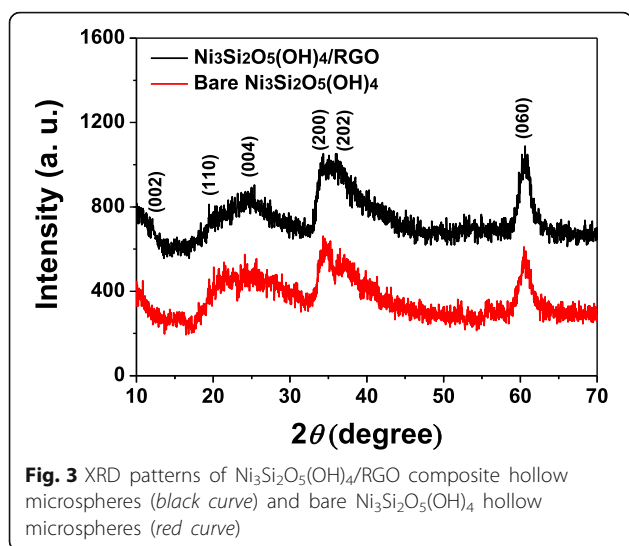
Zhang *et al. Nanoscale Research Letters* (2017) 12:325

Page 4 of 11
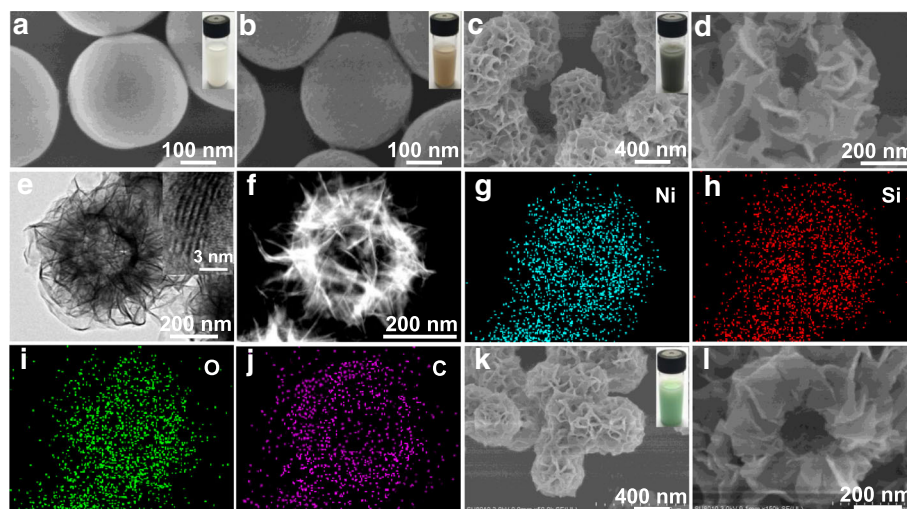
Fig. 2 a, b FESEM images of pristine SiO_2 and SiO_2/GO microspheres, showing the smooth and relatively rougher external surface, respectively; the *insets* in **a** and **b** are digital photographs of the corresponding aqueous suspensions of SiO_2 and SiO_2/GO microspheres, which are pure *white* and *yellow brown* in color, respectively. **c, d** FESEM images of as-prepared $Ni_3Si_2O_5(OH)_4$/RGO composite hollow microspheres at low and high magnifications, respectively; the *inset* in **c** is a digital photograph of their aqueous dispersion, showing dark black in color. **e** TEM image of an individual $Ni_3Si_2O_5(OH)_4$/RGO hollow microsphere; the *inset* is an HRTEM image of a random nanoflake located on its surface, displaying the (002) lattice plane. **f** STEM image of a single $Ni_3Si_2O_5(OH)_4$/RGO hollow microsphere. **g–j** EDS mapping images of elements Ni, Si, O, and C for the $Ni_3Si_2O_5(OH)_4$/RGO microsphere shown in **f. k, l** FESEM images of bare $Ni_3Si_2O_5(OH)_4$ hollow microspheres at low and high magnifications, respectively; the *inset* in **k** is a digital photograph of their aqueous dispersion, exhibiting bright *green* in color

the pristine SiO_2 and SiO_2/GO composite microspheres, $Ni_3Si_2O_5(OH)_4$/RGO microspheres are bigger in size (~600 nm in diameter), and their external surface is composed of plenty of highly curved and wrinkled nanoflakes with the thickness of tens of nanometers (Fig. 2c, d), which should originate from the homogeneous deposition, coverage, and growth of $Ni_3Si_2O_5(OH)_4$ on the substrate microspheres, leading to the hierarchical porous architecture with a flower-like shape. Meanwhile, differing from the apparent colors of pristine SiO_2 and SiO_2/GO composite microspheres, $Ni_3Si_2O_5(OH)_4$/RGO microspheres show a dark color (inset of Fig. 2c), and such deep color is owing to the presence of the RGO component within the sample. Figure 2d exhibits the FESEM image of a typical $Ni_3Si_2O_5(OH)_4$/RGO microsphere with a broken shell, revealing the hollow structure, which was further verified by the following TEM and scanning TEM (STEM) examinations. As exhibited in Fig. 2e, f, an evident interior cavity with a uniform shell thickness of ~150 nm was found in each well-defined $Ni_3Si_2O_5(OH)_4$/RGO microsphere, which is indicative of total removal of the SiO_2 template but without collapse of the hollow structure. The inset of Fig. 2e is a high-resolution TEM (HRTEM) image of an arbitrary $Ni_3Si_2O_5(OH)_4$ nanoflake anchored on a $Ni_3Si_2O_5(OH)_4$/RGO microsphere, where the lattice fringes are visible and the interplanar spacing is calculated to be 0.74 nm, agreeing well with the (002) crystal plane of $Ni_3Si_2O_5(OH)_4$ [9, 16, 17]. The elemental distribution of the $Ni_3Si_2O_5(OH)_4$/RGO

microsphere presented in Fig. 2f was further analyzed by the corresponding EDS mappings. As can be clearly seen in Fig. 2g–j, all the Ni, Si, O, and C signals were detected and filled the microsphere area, demonstrating their homogeneous distribution in this sample. Notably, PVP plays an important role in the hydrothermal synthetic system. In the absence of PVP, although a $Ni_3Si_2O_5(OH)_4$/RGO hybrid material can be fabricated as well, such composite agglomerated seriously and its spherical morphology was rather inferior to that of $Ni_3Si_2O_5(OH)_4$/RGO composite hollow microspheres (Additional file 1: Figure S2). It is assumed that PVP favored the dispersion of substrate microspheres (i.e., the SiO_2/GO microspheres) and effectively alleviated the agglomeration of products during the hydrothermal process, leading to well-defined $Ni_3Si_2O_5(OH)_4$/RGO composite hollow microspheres. Moreover, as a comparison, bare $Ni_3Si_2O_5(OH)_4$ hollow microspheres were hydrothermally fabricated by employing pure SiO_2 microspheres as the template, and the synthetic conditions were identical to those for preparation of $Ni_3Si_2O_5(OH)_4$/RGO microspheres. Obviously, their sphere-like shape, hierarchical morphology, and hollow structure are similar to those of the counterpart (Fig. 2k, l), whereas their apparent color shows bright green (inset of Fig. 2k).
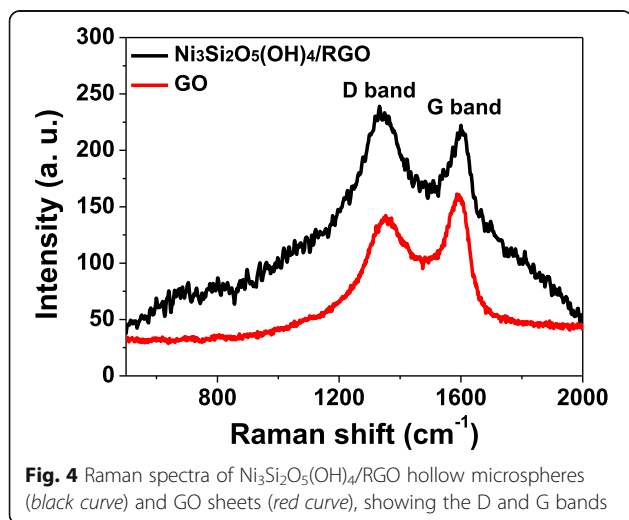
Powder XRD technique was made to characterize the structure and phase information of the products. As shown in the XRD patterns of both $Ni_3Si_2O_5(OH)_4$/RGO microspheres and bare $Ni_3Si_2O_5(OH)_4$ microspheres (Fig. 3), six diffraction peaks are available at

Zhang *et al. Nanoscale Research Letters* (2017) 12:325

Page 5 of 11

Fig. 3 XRD patterns of Ni$_3$Si$_2$O$_5$(OH)$_4$/RGO composite hollow microspheres (*black curve*) and bare Ni$_3$Si$_2$O$_5$(OH)$_4$ hollow microspheres (*red curve*)

around $2\theta = 12.0°$, 19.6°, 24.5°, 34.2°, 36.7°, and 60.5°, which are well indexed to the (002), (110), (004), (200), (202), and (060) crystal planes of pecoraite Ni$_3$Si$_2$O$_5$(OH)$_4$, respectively. These values are in accordance with previous reports and the standard XRD pattern (JCPDS no. 49-1859) as well [9, 10, 15, 17]. Commonly, RGO features a broad diffraction peak at $2\theta = 25°$; nevertheless, in the XRD pattern of Ni$_3$Si$_2$O$_5$(OH)$_4$/RGO microspheres, it is likely to be overlapped by the peaks corresponding to the (110) and (004) crystal planes of the Ni$_3$Si$_2$O$_5$(OH)$_4$ component as a result of the low content and weak diffraction intensity of RGO within Ni$_3$Si$_2$O$_5$(OH)$_4$/RGO microspheres [15, 17].

To verify the existence of the RGO component incorporated in Ni$_3$Si$_2$O$_5$(OH)$_4$/RGO microspheres, the Raman spectra of Ni$_3$Si$_2$O$_5$(OH)$_4$/RGO microspheres and tiny GO sheets were characterized and depicted in Fig. 4. Obviously, there are a couple of bands at around 1350 and 1590 cm^{-1} in both curves, which are ascribed to the characteristic D

Fig. 4 Raman spectra of Ni$_3$Si$_2$O$_5$(OH)$_4$/RGO hollow microspheres (*black curve*) and GO sheets (*red curve*), showing the D and G bands

and G bands of graphene-based species [14, 15, 17]. Generally, the D band arises from the structural defects and edges that damage the symmetry, while the G band refers to the first-order scattering of E_{2g} phonons [4, 14]. Especially, the peak intensity ratio of the D to the G band (I_D/I_G) is a useful measure to evaluate the graphitization degree of carbon matter [4, 14]. The I_D/I_G value for Ni$_3$Si$_2$O$_5$(OH)$_4$/RGO microspheres is 1.08, which is higher than that for GO sheets (0.88), implying that the reduction of GO to RGO indeed occurred during the hydrothermal process, which was undoubtedly incorporated in the final product of Ni$_3$Si$_2$O$_5$(OH)$_4$/RGO microspheres [4, 14, 17].

X-ray photoelectron spectroscopy provides an effective tool for disclosing the surface composition and state of hybrid materials. Figure 5a gives the high-resolution XPS of C 1s of GO sheets. Figure 5b–e shows a set of high-resolution XPS of Ni$_3$Si$_2$O$_5$(OH)$_4$/RGO microspheres for the C 1s, Ni 2p, Si 2p, and O 1s regions, respectively. As envisioned, the detected signals suggest the presence of the four elements in the sample. Both of the C 1s spectra can be resolved into three Gaussian fitted peaks. The peak located at 284.6 eV is attributed to the oxygen-free C=C and C–C bonding, whereas the other two peaks found around 285.6 and 287.1 eV are related to diverse oxygen-containing groups including C–OH, O=C, and C–O–C [23, 24]. The relative intensity of oxygen-containing groups in the C 1s spectrum of Ni$_3$Si$_2$O$_5$(OH)$_4$/RGO microspheres significantly decreased as compared with that in the C 1s spectrum of tiny GO sheets, once again indicating that the immobilized GO sheets wrapping on the substrate microspheres underwent a drastic loss of oxygen-containing groups during the hydrothermal reaction, leading to its reduction to the RGO component [4, 22, 23]. Figure 5c is the high-resolution XPS of Ni 2p of Ni$_3$Si$_2$O$_5$(OH)$_4$/RGO microspheres, where a pair of predominant peaks appear at 856.0 and 873.5 eV, corresponding to the binding energy (BE) of Ni 2p3/2 and Ni 2p1/2, respectively [10, 25]. Two shakeup satellite peaks (denoted as "Sat." in Fig. 5c) close to the spin-orbit doublets are also visible at 862.0 and 880.1 eV with the BE separation of 18.1 eV [10, 25]. All these data agree well with the reported ones and demonstrate the presence of Ni(II) in this sample [10, 25]. Besides, the high-resolution XPS of Si 2p and O 1s reveal strong peaks at 102.3 and 531.3 eV, respectively, which are typical BE values for metal silicate hydroxides as well and mainly derive from the Ni–Si and Si–O bonding [9, 10].

The porous feature of Ni$_3$Si$_2$O$_5$(OH)$_4$/RGO and bare Ni$_3$Si$_2$O$_5$(OH)$_4$ microspheres was surveyed by BET measurements. As shown in their nitrogen adsorption–desorption isotherms (Fig. 6a), both of them can be classified into type IV isotherms with a typical hysteresis

Zhang *et al. Nanoscale Research Letters* (2017) 12:325

Page 6 of 11

Fig. 5 a High-resolution XPS of C 1s of tiny GO sheets. **b–e** High-resolution XPS of $Ni_3Si_2O_5(OH)_4$/RGO hollow microspheres, showing the C 1s, Ni 2p, Si 2p, and O 1s regions, respectively
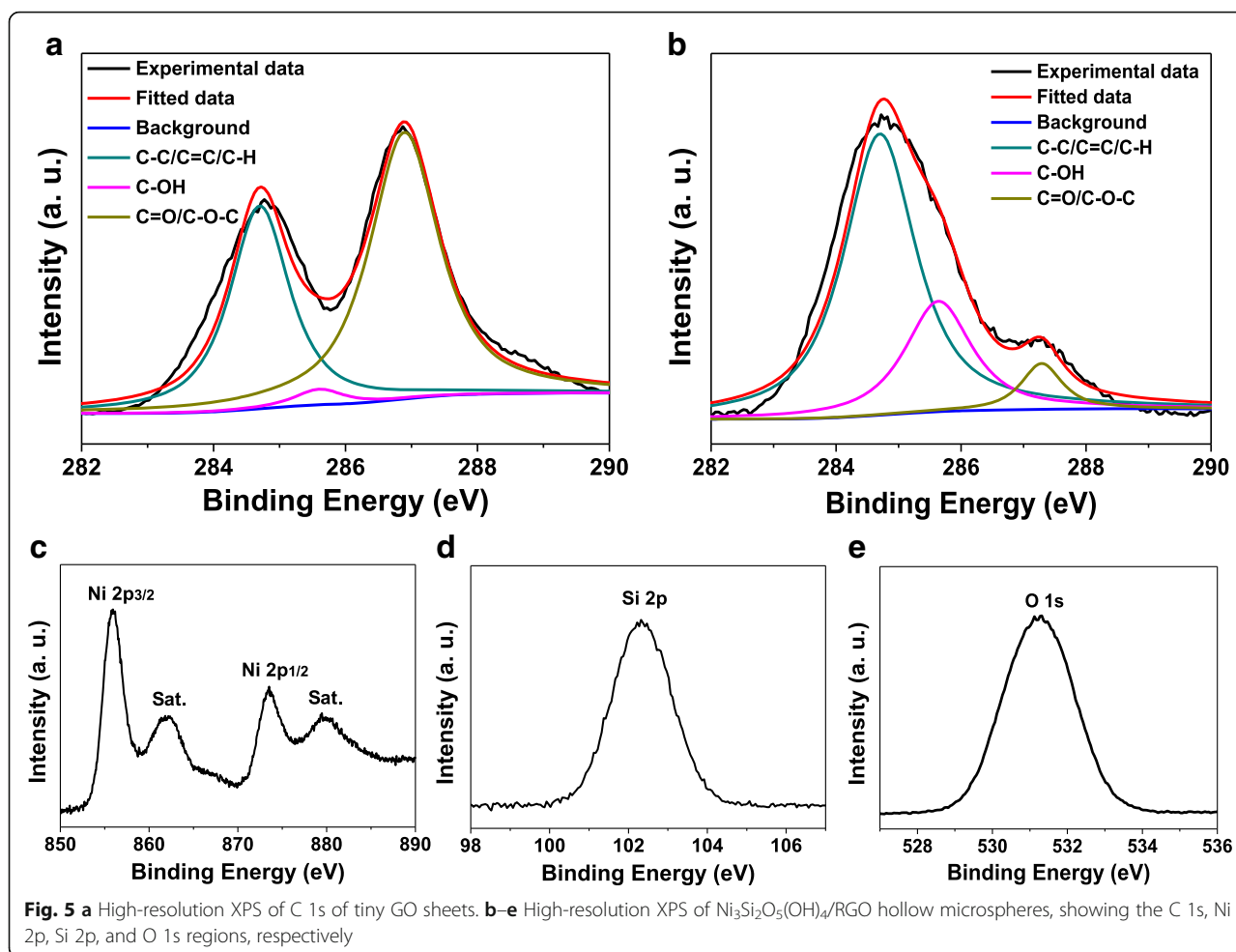
loop ranging from 0.5 to 0.9 P/P_0 in each of them, suggesting the presence of mesopores in the two specimens [4, 26]. Based on the isotherms, the pore size distribution and specific surface area are deduced according to the Barrett–Joyner–Halenda model, and the corresponding plots are presented in Fig. 6b, which once again manifest the existence of well-developed porosity with an average pore size centered around 20 nm and a wide distribution from micro-pores to macropores in both samples [2, 26]. Such result is consistent with their FESEM and TEM observations as well (Fig. 2), and the pores are possibly formed by the complex intertwining and stacking among the nanoflakes [27]. Thanks to the hierarchical porous architecture, the specific surface area of $Ni_3Si_2O_5(OH)_4$/RGO and bare $Ni_3Si_2O_5(OH)_4$ microspheres is as high as 67.6 and 61.6 m^2 g^{-1}, respectively. It is assumed that the larger specific surface area of $Ni_3Si_2O_5(OH)_4$/RGO microspheres would increase the contact area between the electrolyte and electrode material, facilitate the mass transport of c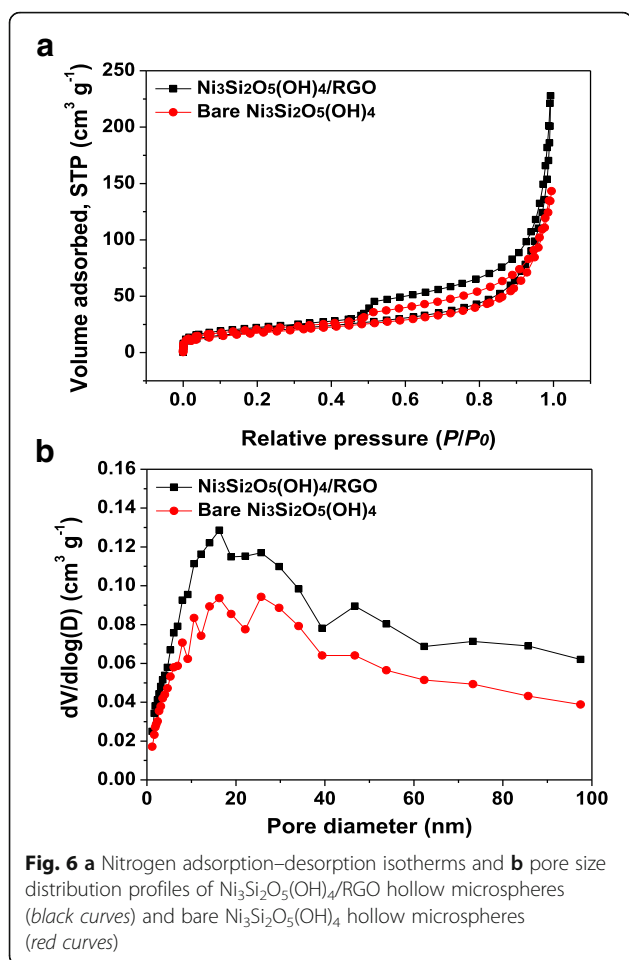harged ions, and provide more reactive sites during electrochemical reactions and thus bring about preferable supercapacitive performance [4, 28, 29].

Electrochemical Investigation

The electrochemical properties of $Ni_3Si_2O_5(OH)_4$/RGO hollow microspheres, bare $Ni_3Si_2O_5(OH)_4$ hollow microspheres, and bare RGO material were evaluated by CV and GCD measurements in a three-electrode system employing aqueous solution of 2 M KOH as the electrolyte. Figure 7a displays their CV curves at the sweeping rate of 20 mV s^{-1}. There are a pair of redox peaks in both CV curves of $Ni_3Si_2O_5(OH)_4$/RGO and bare $Ni_3Si_2O_5(OH)_4$ microspheres, which arise from the transition of nickel ions between different oxidation states [10, 27, 30]:

$$Ni_3^{II}Si_2O_5(OH)_4 + 2OH^- \leftrightarrow Ni_3^{III}Si_2O_5(OH)_6 + 2e^-$$
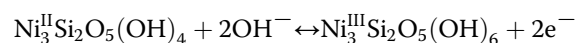
implying their pseudocapacitive characteristics [27, 30], while there are no obvious redox peaks in the CV curve of bare RGO material, suggesting its electric double-layer capacitance nature [2, 4]. The peak current density

Zhang *et al. Nanoscale Research Letters* (2017) 12:325

Page 7 of 11

Fig. 6 a Nitrogen adsorption–desorption isotherms and **b** pore size distribution profiles of $Ni_3Si_2O_5(OH)_4$/RGO hollow microspheres (*black curves*) and bare $Ni_3Si_2O_5(OH)_4$ hollow microspheres (*red curves*)

and the integral area enclosed by the CV curve of $Ni_3Si_2O_5(OH)_4$/RGO hollow microspheres are higher than those of bare $Ni_3Si_2O_5(OH)_4$ hollow microspheres and bare RGO material, indicating the best capacitance [4, 9]. Figure 7b is the CV curves of $Ni_3Si_2O_5(OH)_4$/RGO hollow microspheres at varied scanning rates of 2–100 mV s^{-1}. With elevating sweeping rates, the shape of the CV curves is not remarkably altered and the intensity of redox peaks gradually goes up with only a slight shift toward higher potential, demonstrating that fast electrochemical reactions take place at the interface between the electrolyte and active material and the $Ni_3Si_2O_5(OH)_4$/RGO hollow microsphere electrode possesses excellent rate capability [19, 31]. Figure 7c depicts the GCD curves of $Ni_3Si_2O_5(OH)_4$/RGO, bare $Ni_3Si_2O_5(OH)_4$, and bare RGO electrodes in the potential range of 0.2–0.6 V tested at the current density of 1 A g^{-1}. It is not hard to see that the discharge time of the $Ni_3Si_2O_5(OH)_4$/RGO microsphere electrode is the longest. Such result is consistent with the CV measurements displayed in Fig. 7a and further confirms its superior supercapacitive

behavior. The specific capacitance of a single electrode is able to be obtained on the basis of the equation described as follows:

$$C = i \cdot \Delta t / \Delta V \cdot m$$

where C (F g^{-1}) stands for the specific capacitance, i (A) represents the constant current, t (s) is the discharge time, ΔV (V) is the potential window, and m (g) is the mass of active material [4, 9, 27]. Therefore, the C of $Ni_3Si_2O_5(OH)_4$/RGO microspheres at the current density 1 A g^{-1} is deduced to be 178.9 F g^{-1}, which is clearly higher than that of bare $Ni_3Si_2O_5(OH)_4$ microspheres (138.4 F g^{-1}) and bare RGO material (12.2 F g^{-1}). Figure 7d gives its GCD curves at a group of different current densities, based on which the C of the $Ni_3Si_2O_5(OH)_4$/RGO microsphere electrode is calculated to be 178.9, 166.5, 150.8, 138.9, 132.5, 126.8, 120.1, and 114.4 F g^{-1} at the current density of 1, 2, 3, 4, 5, 6, 8, and 10 A g^{-1}, respectively. The change in its C as a function of current density is also plotted in Fig. 7e. Obviously, the C of the $Ni_3Si_2O_5(OH)_4$/RGO microsphere electrode gradually drops with increasing current density. It is inferred that both the outer and inner pores and reactive sites would contribute to the electrochemical reactions at low current densities, giving rise to high C values, while only the external surface of the electrode material is involved in the charge/discharge processes at high current densities, thus resulting in the diminishment of the C value [4, 29]. Compared with its maximum C at the current density of 1 A g^{-1}, its C at 5 and 10 A g^{-1} maintains as high as 74.1 and 63.9% of the initial one, respectively, indicating prominent rate capability. However, for the bare $Ni_3Si_2O_5(OH)_4$ microsphere electrode, the C at 5 and 10 A g^{-1} decreases to only 57.2 and 47.2% of that at 1 A g^{-1}, respectively, exhibiting inferior rate capability (Additional file 1: Figure S3). It is assumed that two reasons are responsible for the capacitance enhancement and rate capability improvement of the $Ni_3Si_2O_5(OH)_4$/RGO microsphere electrode. On the one hand, $Ni_3Si_2O_5(OH)_4$/RGO microspheres feature a porous hollow structure with a high-level hierarchy and larger specific surface area, which is quite favorable for the rapid transport and adsorption of electrolyte ions inside the electrode material. On the other hand, benefiting from the hybridization of $Ni_3Si_2O_5(OH)_4$ with RGO, the electronic conductivity is significantly improved, thus facilitating more effective electron transport within the $Ni_3Si_2O_5(OH)_4$/RGO microsphere electrode.

To further interpret the enhanced electrochemical behavior of the $Ni_3Si_2O_5(OH)_4$/RGO microsphere electrode, EIS measurements on $Ni_3Si_2O_5(OH)_4$/RGO and bare $Ni_3Si_2O_5(OH)_4$ microsphere electrodes were conducted, and the corresponding Nyquist plots are

Zhang et al. Nanoscale Research Letters (2017) 12:325

Page 8 of 11
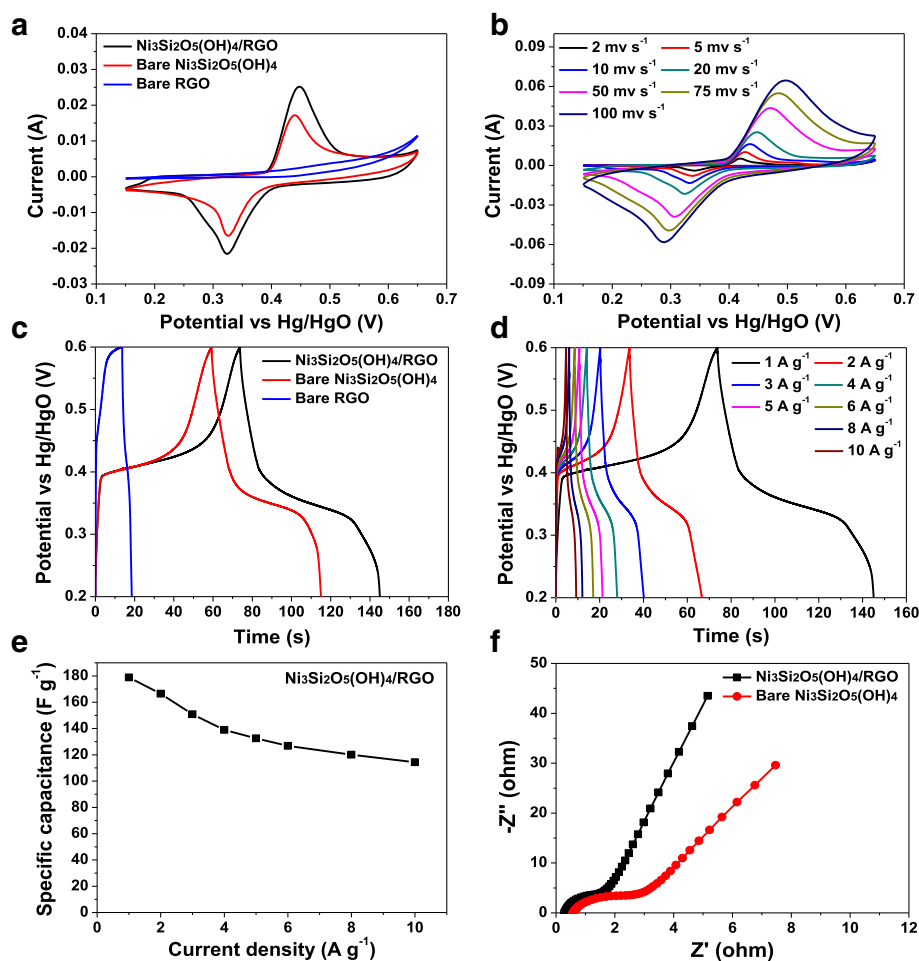
Fig. 7 a CV curves of $Ni_3Si_2O_5(OH)_4$/RGO hollow microspheres (*black curve*), bare $Ni_3Si_2O_5(OH)_4$ hollow microspheres (*red curve*), and bare RGO material (*blue curve*) tested at the scanning rate of 20 mV s^{-1} in 2 M KOH. **b** CV curves of $Ni_3Si_2O_5(OH)_4$/RGO hollow microspheres tested at a series of different sweeping rates. **c** GCD curves of $Ni_3Si_2O_5(OH)_4$/RGO hollow microspheres (*black curve*), bare $Ni_3Si_2O_5(OH)_4$/RGO microspheres (*red curve*) and bare RGO material (*blue curve*) at the current density of 1 A g^{-1}. **d** GCD curves of $Ni_3Si_2O_5(OH)_4$/RGO hollow microspheres measured at a set of varied current densities. **e** Specific capacitance of $Ni_3Si_2O_5(OH)_4$/RGO hollow microsphere electrode deduced from the GCD curves depicted in **d** as a function of current density. **f** Nyquist plots of $Ni_3Si_2O_5(OH)_4$/RGO hollow microsphere (*black curve*) and bare $Ni_3Si_2O_5(OH)_4$ hollow microsphere (*red curve*) electrodes

presented in Fig. 7f. Both of them show a depressed semicircle in the high-frequency region together with a straight line in the low-frequency region. In the high-frequency region, the intercept at the real axis and the diameter of the semicircle represent the equivalent series resistance (R_s) of the electrode and the charge transfer resistance (R_{ct}) at the electrode/electrolyte interface, respectively [32–34]. Apparently, compared with the bare $Ni_3Si_2O_5(OH)_4$ microsphere electrode, the $Ni_3Si_2O_5(OH)_4$/RGO microsphere electrode possesses much smaller R_s and R_{ct} values, which are indeed indicative of its better electronic conductivity and allow for faster electron transport within the electrode matrix [32–34]. In the low-frequency region, the straight line reflects the Warburg impedance, which can be used to describe the diffusive resistance

of electrolyte ions [32–34]. The $Ni_3Si_2O_5(OH)_4$/RGO microsphere electrode shows a higher slope than the bare $Ni_3Si_2O_5(OH)_4$ microsphere electrode in the linear part, suggesting more rapid ion diffusion inside it [32–34]. These EIS findings further support and verify the abovementioned analyses on the excellent electrochemical performances of the $Ni_3Si_2O_5(OH)_4$/RGO microsphere electrode.

Cycle life plays a key role in the application of electrode materials in supercapacitors, since little change in their capacitance would make the supercapacitors work steadily and safely [27]. The cyclic performance of the $Ni_3Si_2O_5(OH)_4$/RGO microsphere electrode was determined by repetitive GCD measurements for up to 5000 cycles at the current density of 6 A g^{-1} (Fig. 8a, b). As continuous charging/discharging proceeds, the

Zhang *et al. Nanoscale Research Letters* (2017) 12:325

Page 9 of 11
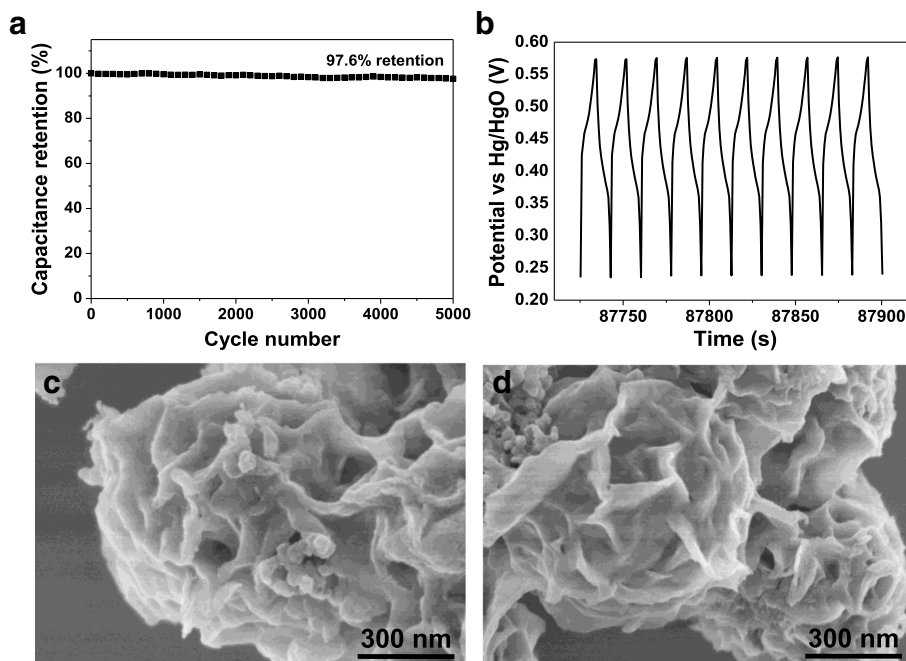
Fig. 8 a Cyclic performance of $Ni_3Si_2O_5(OH)_4$/RGO microsphere electrode at the current density of 6 A g^{-1} for up to 5000 cycles. **b** The charge/discharge curve of $Ni_3Si_2O_5(OH)_4$/RGO microsphere electrode for the last 10 cycles. **c, d** FESEM images of $Ni_3Si_2O_5(OH)_4$/RGO microsphere electrode after charging/discharging for 5000 cycles

capacitance decays quite slowly (Fig. 8a), and the shape of the GCD curve for the last 10 cycles remains good enough (Fig. 8b). The capacitance retention of the electrode even reaches up to 97.6% after the whole tests, which is preferable or comparable to a number of nickel-based supercapacitor electrode materials reported previously (Table 1). Besides, the $Ni_3Si_2O_5(OH)_4$/RGO

microsphere electrode after such tests was subjected to FESEM examinations as well, which disclosed the hierarchical porous architecture with spherical morphology freed from significant collapse and deformation (Fig. 8c, d). The structural integrity during the repetitive charging/discharging process largely contributes to the capacitance retention and convincingly demonstrates the

Table 1 Comparison of cycling stability between $Ni_3Si_2O_5(OH)_4$/RGO composite hollow microspheres and some of other reported nickel-based electrode materials. All these data were obtained in three-electrode systems

Electrode materials	Current density (A g^{-1})	Number of cycles	Capacitance retention (%)	Ref.
$Ni_3Si_2O_5(OH)_4$/RGO composite hollow microspheres	6	5000	97.6	This work
NiO nanoparticles	2	1000	60.6	[35]
NiO nanosheet hollow spheres	3	1000	91	[36]
Nanoporous $Ni(OH)_2$	1	2000	92.3	[37]
Porous $Ni(OH)_2$/NiOOH composite film	2	1000	81	[38]
Doughnut-like $Ni(OH)_2$–$Co(OH)_2$ composites	5	1000	84.7	[39]
$Ni(OH)_2$–Ni nanohybrids	5	2000	98.4	[40]
Mesoporous $NiCo_2O_4$ nanosheets	2	2400	94	[41]
Urchin-like $NiCo_2O_4$ nanostructures	8	2000	90.8	[42]
Mesoporous $Ni_{0.3}Co_{2.7}O_4$ hierarchical structures	0.625	3000	98.1	[43]
RGO/$NiCo_2O_4$ nanoflake composites	4	2000	90.8	[44]
$NiCo_2S_4$ ball-in-ball hollow spheres	5	2000	87	[45]

Zhang *et al. Nanoscale Research Letters* (2017) 12:325

Page 10 of 11

splendid cycling stability, durability, and application potential in practical supercapacitors.

Conclusions

In summary, GO-encapsulated SiO_2 microspheres were prepared by sonication-assisted interfacial self-assembly of tiny GO sheets on positively charged SiO_2 microspheres. By employing the resulting SiO_2/GO composite microspheres as the template and silicon source, $Ni_3Si_2O_5(OH)_4$/RGO composite hollow microspheres were one-pot hydrothermally synthesized, which possessed unique hierarchical porous architecture with a large surface area. When used as a supercapacitor electrode material, $Ni_3Si_2O_5(OH)_4$/RGO composite hollow microspheres delivered a maximum specific capacitance of 178.9 F g^{-1} at the current density of 1 A g^{-1}, which was better than that of currently developed contrastive bare $Ni_3Si_2O_5(OH)_4$ hollow microspheres and bare RGO material, exhibiting enhanced supercapacitive property. Of note, the $Ni_3Si_2O_5(OH)_4$/RGO microspheres had salient rate capability and long-term cycling stability, which maintained 97.6% of the initial capacitance after continuous charge/discharge for up to 5000 cycles, displaying a remarkably supercapacitive advantage over lots of other reported nickel-based materials. These results testify that $Ni_3Si_2O_5(OH)_4$/RGO composite hollow microspheres are a promising candidate for high-performance energy storage devices and systems. Moreover, we also anticipate that the present self-template synthetic strategy would be adopted to develop more and more other metal silicate-based materials with distinct morphologies and structures for important applications in various fields.

Additional file

Additional file 1: The experimental details for synthesis of SiO_2 microspheres and SiO_2/GO composite microspheres. Figure S1 (a, b) FESEM images of pristine SiO_2 microspheres at low and high magnifications, respectively. (c, d) FESEM images of SiO_2/GO composite microspheres at low and high magnifications, respectively. Figure S2 FESEM images of $Ni_3Si_2O_5(OH)_4$/RGO hybrid material synthesized in the absence of PVP. Figure S3 (a) GCD curves of bare $Ni_3Si_2O_5(OH)_4$ hollow microspheres measured at a set of varied current densities. (b) Specific capacitance of bare $Ni_3Si_2O_5(OH)_4$ hollow microsphere electrode deduced from the GCD curves depicted in (a) as a function of current density. (DOCX 5399 kb)

Abbreviations

BE: Binding energy; BET: Brunauer–Emmett–Teller; CV: Cyclic voltammetry; EDS: Energy-dispersive spectroscopy; EIS: Electrochemical impedance spectroscopy; FESEM: Field emission scanning electron microscopy; GCD: Galvanostatic charge/discharge; GO: Graphene oxide; HRTEM: High-resolution transmission electron microscopy; NMP: *N*-Methyl-2-pyrrolidone; PDDA: Poly(diallyldimethylammonium) chloride; PVDF: Polyvinylidene fluoride; PVP: Polyvinylpyrrolidone; RGO: Reduced graphene oxide; STEM: Scanning TEM; TEM: Transmission electron microscopy; XPS: X-ray photoelectron spectra; XRD: X-ray diffraction

Authors' Contributions

WX conceived this research and revised the manuscript. LT designed the experimental strategy. YZ, WZ, and HY carried out most of the experiments. TF, YP, and HL analyzed the data and drafted this paper. All authors read and approved the final manuscript.

Competing Interests

The authors declare that they have no competing interests.

Publisher's Note

Springer Nature remains neutral with regard to jurisdictional claims in published maps and institutional affiliations.

References

1. Wang Y, Song Y, Xia Y (2016) Electrochemical capacitors: mechanism, materials, systems, characterization and applications. Chem Soc Rev 45:5925–5950
2. Yi H, Wang H, Jing Y, Peng T, Wang Y, Guo J, He Q, Guo Z, Wang X (2015) Advanced asymmetric supercapacitors based on CNT@Ni(OH)$_2$ core–shell composites and 3D graphene networks. J Mater Chem A 3:19545–19555
3. Liu Y, Shi Z, Gao Y, An W, Cao Z, Liu J (2016) Biomass-swelling assisted synthesis of hierarchical porous carbon fiber for supercapacitor electrodes. ACS Appl Mater Interfaces 8:28283–28290
4. Xiao W, Zhou W, Feng T, Zhang Y, Liu H, Tian L (2016) Simple synthesis of molybdenum disulfide/reduced graphene oxide composite hollow microspheres as supercapacitor electrode material. Materials 9:783
5. Zang X, Dai Z, Yang J, Zhang Y, Huang W, Dong X (2016) Template-assisted synthesis of nickel sulfide nanowires: tuning the compositions for supercapacitors with improved electrochemical stability. ACS Appl Mater Interfaces 8:24645–24651
6. Zhu SJ, Jia JQ, Wang T, Zhao D, Yang J, Dong F, Guo Z, Shang ZG, Zhang YX (2015) Rational design of octahedron and nanowire CeO$_2$@MnO$_2$ core–shell heterostructures with outstanding rate capability for asymmetric supercapacitors. Chem Commun 51:14840–14843
7. Liu Y, Wang W, Huang H, Gu L, Wang Y, Peng X (2014) The highly enhanced performance of lamellar WS$_2$ nanosheet electrodes upon intercalation of single-walled carbon nanotubes for supercapacitors and lithium ions batteries. Chem Commun 50:4485–4488
8. Yu Z, Tetard L, Zhai L, Thomas J (2015) Supercapacitor electrode materials: nanostructures from 0 to 3 dimensions. Energy Environ Sci 8:702–730
9. Rong Q, Long L-L, Zhang X, Huang Y-X, Yu H-Q (2015) Layered cobalt nickel silicate hollow spheres as a highly-stable supercapacitor material. Appl Energy 153:63–69
10. Qiu C, Jiang J, Ai L (2016) When layered nickel–cobalt silicate hydroxide nanosheets meet carbon nanotubes: a synergetic coaxial nanocable structure for enhanced electrocatalytic water oxidation. ACS Appl Mater Interfaces 8:945–951
11. Zhang S, Gao H, Li J, Huang Y, Alsaedi A, Hayat T, Xu X, Wang X (2017) Rice husks as a sustainable silica source for hierarchical flower-like metal silicate architectures assembled into ultrathin nanosheets for adsorption and catalysis. J Hazard Mater 321:92–102
12. Kuznicki SM, Bell VA, Nair S, Hillhouse HW, Jacubinas RM, Braunbarth CM, Toby BH, Tsapatsis M (2001) A titanosilicate molecular sieve with adjustable pores for size-selective adsorption of molecules. Nature 412:720–724
13. Fang Q, Xuan S, Jiang W, Gong X (2011) Yolk-like micro/nanoparticles with superparamagnetic iron oxide cores and hierarchical nickel silicate shells. Adv Funct Mater 21:1902–1909

Zhang *et al. Nanoscale Research Letters* (2017) 12:325

Page 11 of 11

14. Gui C-X, Wang Q-Q, Hao S-M, Qu J, Huang P-P, Cao C-Y, Song W-G, Yu Z-Z (2014) Sandwichlike magnesium silicate/reduced graphene oxide nanocomposite for enhanced Pb^{2+} and methylene blue adsorption. ACS Appl Mater Interfaces 6:14653–14659

15. Tang C, Sheng J, Xu C, Khajehbashi SMB, Wang X, Hu P, Wei X, Wei Q, Zhou L, Mai L (2015) Facile synthesis of reduced graphene oxide wrapped nickel silicate hierarchical hollow spheres for long-life lithium-ion batteries. J Mater Chem A 3:19427–19432

16. Gui C-X, Hao S-M, Liu Y, Qu J, Yang C, Yu Y, Wang Q-Q, Yu Z-Z (2015) Carbon nanotube@layered nickel silicate coaxial nanocables as excellent anode materials for lithium and sodium storage. J Mater Chem A 3:16551–16559

17. Wang Q-Q, Qu J, Liu Y, Gui C-X, Hao S-M, Yu Y, Yu Z-Z (2015) Growth of nickel silicate nanoplates on reduced graphene oxide as layered nanocomposites for highly reversible lithium storage. Nanoscale 7: 16805–16811

18. Yu P, Li Y, Zhao X, Wu L, Zhang Q (2014) Graphene-wrapped polyaniline nanowire arrays on nitrogen-doped carbon fabric as novel flexible hybrid electrode materials for high-performance supercapacitor. Langmuir 30:5306–5313

19. Numan A, Duraisamy N, Omar FS, Mahipal YK, Ramesh K, Ramesh S (2016) Enhanced electrochemical performance of cobalt oxide nanocube intercalated reduced graphene oxide for supercapacitor application. RSC Adv 6:34894–34902

20. Lee T, Min SH, Gu M, Jung YK, Lee W, Lee JU, Seong DG, Kim BS (2015) Layer-by-layer assembly for graphene-based multilayer nanocomposites: synthesis and applications. Chem Mater 27:3785–3796

21. Xiao W, Zhang Y, Liu B (2015) Raspberrylike SiO_2@reduced graphene oxide@AgNP composite microspheres with high aqueous dispersity and excellent catalytic activity. ACS Appl Mater Interfaces 7:6041–6046

22. Xiao W, Zhang Y, Tian L, Liu H, Liu B, Pu Y (2016) Facile synthesis of reduced graphene oxide/titania composite hollow microspheres based on sonication-assisted interfacial self-assembly of tiny graphene oxide sheets and the photocatalytic property. J Alloys Compd 665:21–30

23. Zhang Z, Xiao F, Guo Y, Wang S, Liu Y (2013) One-pot self-assembled three-dimensional TiO_2-graphene hydrogel with improved adsorption capacities and photocatalytic and electrochemical activities. ACS Appl Mater Interfaces 5:2227–2233

24. Cao J, Liu Q, Han D, Yang S, Yang J, Wang T, Niu H (2014) Highly enhanced photocatalytic properties of ZnS nanowires–graphene nanocomposites. RSC Adv 4:30798–30806

25. Niu H, Zhou D, Yang X, Li X, Wang Q, Qu F (2015) Towards three-dimensional hierarchical ZnO nanofiber@Ni(OH)$_2$ nanoflake core–shell heterostructures for high-performance asymmetric supercapacitors. J Mater Chem A 3:18413–18421

26. Zhu Y, Ji X, Wu Z, Liu Y (2015) $NiCo_2S_4$ hollow microspheres decorated by acetylene black for high-performance asymmetric supercapacitor. Electrochim Acta 186:562–571

27. Zhao J, Zhang Y, Wang T, Li P, Wei C, Pang H (2015) Reed leaves as a sustainable silica source for 3D mesoporous nickel (cobalt) silicate architectures assembled into ultrathin nanoflakes for high-performance supercapacitors. Adv Mater Interfaces 2:1400377

28. Thangappan R, Kalaiselvam S, Elayaperumal A, Jayavel R, Arivanandhan M, Karthikeyan R, Hayakawa Y (2016) Graphene decorated with MoS_2 nanosheets: a synergetic energy storage composite electrode for supercapacitor applications. Dalton Trans 45:2637–2646

29. Wang L, Ma Y, Yang M, Qi Y (2015) Hierarchical hollow MoS_2 nanospheres with enhanced electrochemical properties used as an electrode in supercapacitor. Electrochim Acta 186:391–396

30. Zhao J, Zheng M, Run Z, Xia J, Sun M, Pang H (2015) 1D $Co_{2.18}Ni_{0.82}Si_2O_5(OH)_4$ architectures assembled by ultrathin nanoflakes for high-performance flexible solid-state asymmetric supercapacitors. J Power Sources 285:385–392

31. Duraisamy N, Numan A, Ramesh K, Choi K-H, Ramesh S, Ramesh S (2015) Investigation on structural and electrochemical properties of binder free nanostructured nickel oxide thin film. Mater Lett 161:694–697

32. Ji H, Liu C, Wang T, Chen J, Mao Z, Zhao J, Hou W, Yang G (2015) Porous hybrid composites of few-layer MoS_2 nanosheets embedded in a carbon matrix with an excellent supercapacitor electrode performance. Small 11:6480–6490

33. Shi D, Zhang L, Yin X, Huang TJ, Gong H (2016) A one step processed advanced interwoven architecture of Ni(OH)$_2$ and Cu nanosheets with ultrahigh supercapacitor performance. J Mater Chem A 4:12144–12151

34. Zhang Y, Sun W, Rui X, Li B, Tan HT, Guo G, Madhavi S, Zong Y, Yan Q (2015) One-pot synthesis of tunable crystalline Ni_3S_4@amorphous MoS_2 core/shell nanospheres for high-performance supercapacitors. Small 11:3694–3702

35. Jahromi SP, Pandikumar A, Goh BT, Lim YS, Basirun WJ, Lim HN, Huang NM (2015) Influence of particle size on performance of a nickel oxide nanoparticle-based supercapacitor. RSC Adv 5:14010–14019

36. Ding S, Zhu T, Chen JS, Wang Z, Yuan C, Lou XW (2011) Controlled synthesis of hierarchical NiO nanosheet hollow spheres with enhanced supercapacitive performance. J Mater Chem 21:6602–6606

37. Hu G, Li C, Gong H (2010) Capacitance decay of nanoporous nickel hydroxide. J Power Sources 195:6977–6981

38. Yuan YF, Xia XH, Wu JB, Yang JL, Chen YB, Guo SY (2011) Nickel foam-supported porous Ni(OH)$_2$/NiOOH composite film as advanced pseudocapacitor material. Electrochim Acta 56:2627–2632

39. Li J, Yang M, Wei J, Zhou Z (2012) Preparation and electrochemical performances of doughnut-like Ni(OH)$_2$–Co(OH)$_2$ composites as pseudocapacitor materials. Nanoscale 4:4498–4503

40. Zhao J, He J, Sun M, Qu M, Pang H (2015) Nickel hydroxide–nickel nanohybrids indirectly from coordination microfibers of high-performance supercapacitor electrodes. Inorg Chem Front 2:129–135

41. Yuan C, Li J, Hou L, Zhang X, Shen L, Lou XW (2012) Ultrathin mesoporous $NiCo_2O_4$ nanosheets supported on Ni foam as advanced electrodes for supercapacitors. Adv Funct Mater 22:4592–4597

42. Wang Q, Liu B, Wang X, Ran S, Wang L, Chen D, Shen G (2012) Morphology evolution of urchin-like $NiCo_2O_4$ nanostructures and their applications as psuedocapacitors and photoelectrochemical cells. J Mater Chem 22:21647–21653

43. Wu HB, Pang H, Lou XW (2013) Facile synthesis of mesoporous $Ni_{0.3}Co_{2.7}O_4$ hierarchical structures for high-performance supercapacitors. Energy Environ Sci 6:3619–3626

44. Wang L, Wang X, Xiao X, Xu F, Sun Y, Li Z (2013) Reduced graphene oxide/nickel cobaltite nanoflake composites for high specific capacitance supercapacitors. Electrochim Acta 111:937–945

45. Shen L, Yu L, Wu HB, Yu X-Y, Zhang X, Lou XW (2015) Formation of nickel cobalt sulfide ball-in-ball hollow spheres with enhanced electrochemical pseudocapacitive properties. Nat Commun 6:6694